PNAS

Structure and supramolecular organization of the canine distemper virus attachment glycoprotein

David Kalbermatter[a,1] [ID], Jean-Marc Jeckelmann[a,1] [ID], Marianne Wyss[b], Neeta Shrestha[b], Dimanthi Pliatsika[c] [ID], Rainer Riedl[c] [ID], Thomas Lemmin[a,1,2] [ID], Philippe Plattet[b,1,2] [ID], and Dimitrios Fotiadis[a,1,2] [ID]

Canine distemper virus (CDV) is an enveloped RNA morbillivirus that triggers respiratory, enteric, and high incidence of severe neurological disorders. CDV induces devastating outbreaks in wild and endangered animals as well as in domestic dogs in countries associated with suboptimal vaccination programs. The receptor-binding tetrameric attachment (H)-protein is part of the morbilliviral cell entry machinery. Here, we present the cryo-electron microscopy (cryo-EM) structure and supramolecular organization of the tetrameric CDV H-protein ectodomain. The structure reveals that the morbilliviral H-protein is composed of three main domains: stalk, neck, and heads. The most unexpected feature was the inherent asymmetric architecture of the CDV H-tetramer being shaped by the neck, which folds into an almost 90° bent conformation with respect to the stalk. Consequently, two non-contacting receptor-binding H-head dimers, which are also tilted toward each other, are located on one side of an intertwined four helical bundle stalk domain. Positioning of the four protomer polypeptide chains within the neck domain is guided by a glycine residue (G158), which forms a hinge point exclusively in two protomer polypeptide chains. Molecular dynamics simulations validated the stability of the asymmetric structure under near physiological conditions and molecular docking showed that two receptor-binding sites are fully accessible. Thus, this spatial organization of the CDV H-tetramer would allow for concomitant protein interactions with the stalk and head domains without steric clashes. In summary, the structure of the CDV H-protein ectodomain provides new insights into the morbilliviral cell entry system and offers a blueprint for next-generation structure-based antiviral drug discovery.

canine distemper virus | cryo-electron microscopy | morbillivirus cell entry | H-protein ectodomain | structure

The human pathogen measles virus (MeV) and the animal pathogen canine distemper virus (CDV) belong to the genus *morbillivirus* of the family *Paramyxoviridae*. Although available vaccines can efficiently prevent both infectious diseases, MeV still causes more than 200,000 deaths per year (1), while CDV continuously induces devastating outbreaks in wild animal species (2–6). Both pathogens trigger respiratory and enteric disorders. However, high incidence of severe neurological dysfunctions is exclusively associated with CDV infections (7–9). These last years, and likely further amplified by the severe acute respiratory syndrome coronavirus-2 (SARS-CoV-2) pandemic, drops in vaccination coverage resulted in measles re-emergence (10), which inevitably delays the global measles eradication program planned by the World Health Organization (WHO). On the other hand, CDV can infect a wide variety of animals, including monkeys (11), which indicates a potential spillover to humans in a putative post-measles era. Noteworthy, CDV can also affect endangered species, as recently exemplified in the panda population (12–14). Pharmacological control of both diseases is therefore urgently needed, since such countermeasures may i) support vaccination campaigns by contributing to fill herd immunity gaps, ii) offer alternative clinical treatments to healthcare systems for disease management, and iii) potentially contribute to species preservation. Although attractive candidates are under development, no Food and Drug Administration (FDA)-approved anti-morbilliviral drug is currently available.

The morbillivirus cell entry machinery, which is composed of two interacting envelope glycoproteins, represents the main target of the host immune response. The tetrameric (composed of a dimer of dimers) attachment (H) protein binds to a cognate host cell surface receptor [signaling lymphocytic activation molecule (CD150/SLAM) in immune cells (15–17) or Nectin-4 in epithelial cells (18, 19)], whereas the trimeric fusion (F) protein fuses the viral envelope with the host cell plasma membrane to ultimately introduce the genetic information into the host cell cytoplasm. It has been suggested that the morbilliviral

Significance

Canine distemper virus (CDV) is an enveloped RNA morbillivirus related to the human pathogen measles virus. CDV induces severe outbreaks in wild and endangered animals as well as in domestic dogs when vaccination programs are suboptimal. A key component of the morbilliviral cell entry machinery is the receptor-binding H-protein. Here, we report the cryo-EM structure of the CDV H-protein ectodomain, which is characterized by three main domains (heads, neck, and stalk) folding in an asymmetric conformational state. Remarkably, the asymmetric structure enables concomitant protein interactions with the stalk and head domains, potentially corresponding to a pre-receptor-bound state. In summary, our structure not only sheds light on the morbilliviral cell entry system, but also lays the groundwork for developing novel antivirals.

[1]D.K., J.-M.J., T.L., P.P., and D.F. contributed equally to this work.

[2]To whom correspondence may be addressed. Email: thomas.lemmin@ibmm.unibe.ch, philippe.plattet@vetsuisse.unibe.ch, or dimitrios.fotiadis@ibmm.unibe.ch.

cell entry mechanism relies on significant structural rearrangements (20, 21). Initially, the H-protein may undergo conformational changes triggered by the receptor engagement, leading to the activation of interacting trimeric F complex. The F-protein is then proposed to refold from a metastable prefusion state into a highly stable postfusion state thereby inducing the fusion of the viral and the host lipid membranes, and thus enabling cell entry.

Rational design of cell entry inhibitors relies on a precise functional and structural understanding of the H/F-mediated membrane fusion process. Although structures of entire soluble morbilliviral prefusion F-ectodomains are available (22, 23), structures of full H-ectodomains are still lacking. Functional (MeV and CDV) and structural (MeV) studies determined three main regions encompassed within the H-ectodomain: a membrane-proximal stalk region (no structure available), a connecting region (no structure available), and a membrane-distal globular receptor-binding head region (apo and receptor-bound structures available) (24–29). The head domains were captured as monomers, dimers, and even tetramers (30–34). The relevance of each of those oligomeric states and conformations with respect to the proposed dynamic cell entry process remains to be demonstrated. Interestingly, functional studies suggested that a segment of the morbilliviral H-stalk region is responsible for direct binding to prefusion F-trimers (29, 35, 36). For morbilliviruses, it is assumed that H and F glycoproteins assemble in a complex prior to receptor contacts (37–39). Although different mechanisms for F activation may occur (20, 21, 40), structures of receptor-binding protein ectodomains of related paramyxoviruses inferred that head domains may prevent interaction with F through steric clashes. In turn, receptor-mediated conformational changes in the receptor-binding protein would be required to enable the formation of the envelope glycoprotein complex (41–43). Hence, elucidating the structures of the morbilliviral stalk and connecting region as well as the spatial positioning of those three domains with each other prior to receptor binding (i.e., in the absence of receptor) is of major importance not only to shed further light into the mechanism of morbilliviral membrane fusion activity, but to refine our understanding of

immunity directed toward the H-protein. Furthermore, the apo structure of the morbilliviral H-tetramer may additionally offer a blueprint for the structure-based design of novel antivirals.

In this study, we determined the cryo-electron microscopy (cryo-EM) structure of the tetrameric H glycoprotein ectodomain of the A75/17 wild-type neurovirulent CDV strain. CDV A75/17 belongs to the America-2 lineage and is closely related to the virulent 5804P CDV strain, which is regularly employed to investigate morbilliviral-induced pathogenesis in animal models (44–51). The overall architecture of the H-ectodomain is characterized by an asymmetric dimer of H-head dimers. The region connecting the heads to the stalk, called the neck domain, is composed of highly interlaced and covalently linked polypeptide segments from each protomer. The neck directs both dimeric head domains in a bent state on one side of the stalk. This asymmetric conformation would allow for concomitant protein interactions with the stalk and head domains without steric clashes.

Results

Overall Architecture of the CDV H-Tetramer. The structure and supramolecular organization of the tetrameric CDV attachment protein H-ectodomain was determined by cryo-EM and single particle 3D reconstruction. A Coulomb potential density (hereinafter referred to as density) map was obtained at an overall resolution of 3.3 Å (*SI Appendix*, Table S1) revealing a wide Y-shaped structure of ~100 Å in depth and ~150 Å in height (*SI Appendix*, Fig. S1). Strikingly, the CDV H-tetramer appears to be asymmetric, consisting of a dimer of dimers. For each protomer, the three main domains of the H-ectodomain, i.e., heads, neck, and stalk, are clearly defined in the map as well as a density arising from the engineered GCN4-domain (*SI Appendix*, Fig. S1). From the density map, an atomic model of the four heads and the neck was built (Fig. 1). The density of the N-terminal stalk was not of sufficient quality for the reliable model building of amino acid side chains. Instead, a poly-alanine (poly-A) model was successfully assembled for the stalk region, which unveiled a
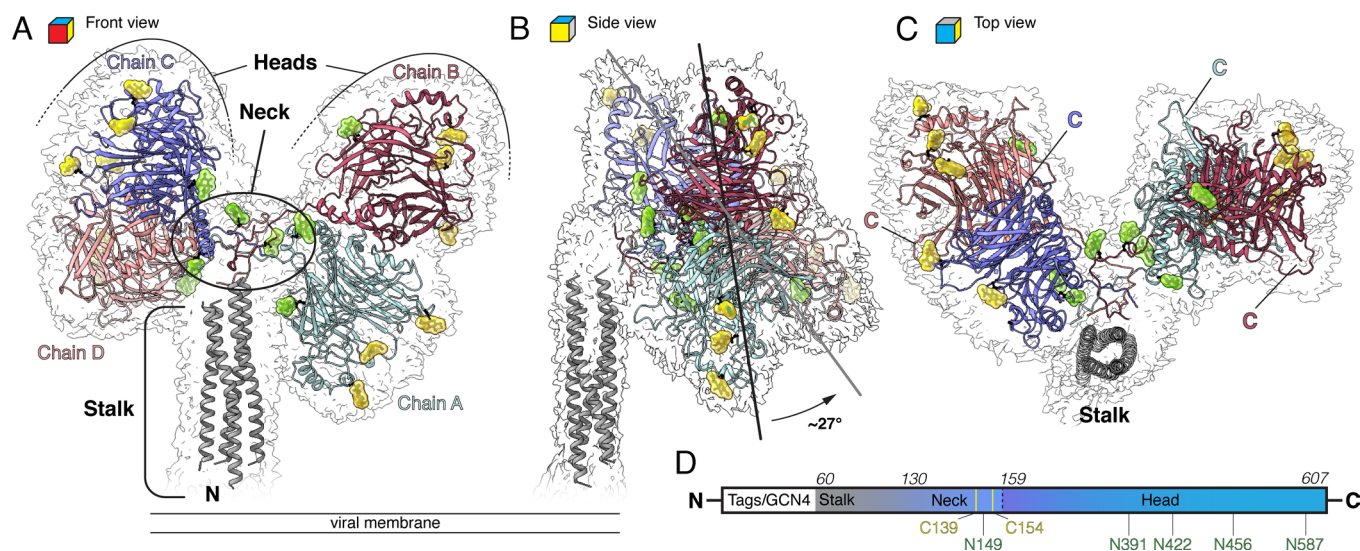

Fig. 1. Structure and supramolecular organization of the tetrameric CDV attachment protein H-ectodomain. Displayed is the cryo-EM map-derived model, oriented such that the stalk is parallel to the viral membrane normal and viewed from the front (*A*), side (*B*), and top (*C*). (*D*) Schematic representation of the CDV H construct used in this study highlighting the N-terminal Tag/GCN4-domain (white), the stalk region (gray), followed by the neck and the head domain (blue hue). Above, corresponding amino acid residue numbers are given in italic. Below, residue numbers involved in disulfide bridge formation and N-glycosylation are indicated. In panels (*A–C*), the structural model is represented as ribbon and color-coded as follows: stalk (gray), neck, and heads (chain A, cyan; chain B, red; chain C, blue; chain D, pink). Individual structural elements and termini are labeled. Glycosylation sites in the model are visualized by molecular volumes of N-acetylglucosamines colored in light green (cryo-EM density present) and yellow (no visible cryo-EM density). In panel (*B*), the ~27° rotation of the chain A/B to C/D dimeric head domains is displayed. The density in panels (*A–C*) is shown at a threshold level of 0.30 (2.16 σ).

characteristic intertwining of four helical structures that would point N-terminally toward the viral membrane (Fig. 1). The neck region that bridges the stalk and the heads contributes with the stalk to the stabilization of the tetramer. In the absence of the membrane domain, stabilization of the tetrameric H-ectodomain was further supported by the tetramerization motif (GCN4) (52, 53) (*Methods* and *SI Appendix*, Fig. S1). Finally, each protomer contains at its C terminus a prominent, globular β-propeller head domain (Fig. 1 and *SI Appendix*, Fig. S2).

Structure and Organization of Head and Neck Domains. Each of the four C-terminal head domains forms a six-bladed β-propeller (*SI Appendix*, Fig. S2) with four experimentally confirmed N-linked glycosylations at positions N391, N422, N456, and N587 (54) (Fig. 1*D*). In the cryo-EM structure, possible densities for a glycan were visible in the vicinity of N391. Head domains also contain a region connecting the β-propeller to the neck that is composed of a loop and a slightly bent α-helical structure (see "connector segment" in *SI Appendix*, Fig. S2). The CDV H-tetramer is organized as a pair of dimeric heads, i.e., chains A–B and C–D (Fig. 1), each composed of two globular head domains organized in a head-to-head fashion. The dimerization interface of a dimeric head is mainly composed of residues located in the β-propeller 2 (β-2), the connector segment, and an α-helical element located between β-1 and β-2 (*SI Appendix*, Fig. S2). The contact region between each protomer was calculated with the Proteins, Interfaces, Structures and Assemblies server (55) and represents about 8% of the total monomeric CDV H surface area (~1,620 Å²). The relative spatial organization of the head dimers is new and characterized by an intrinsic asymmetry. When the CDV H-tetramer is oriented, so that the stalk is parallel to the viral membrane normal, the relative rotational shift between chains A–B and C–D dimers is about 27° (Fig. 1*B*).

The head dimers are connected through the neck domain, which is composed of four polypeptide chains being contributed by all protomers (Fig. 2*A*). The neck is stabilized by hydrogen bonds, hydrophobic interactions, and four interprotomer disulfide bridges between pairs of C139 and C154 residues from chains A–B to chains C–D, respectively (Fig. 2*A* and *SI Appendix*, Fig. S3). Spatial alignments of corresponding chains in the neck domain unveil a structural symmetry between chains A and C, and B and D, respectively (Fig. 2*B*). The main difference between the chains occurs at a hinge point at residue/position G158. In chains A and C, the neck polypeptide forms an extended helix between F150 and G180, while in chains B and D, the helix is unwound from F150 to G158, and kinked by about 90° at G158 (Fig. 2*C* and *SI Appendix*, Figs. S3 and S4). Indeed, the backbone torsional angles of G158 switch from a helical conformation [($\phi \approx -64$; $\psi \approx -42$) in chains A and C] to an extended conformation [($\phi \approx -68$; $\psi \approx 162$) in chains B and D]. More important, the hinge point in chains B and D enables all four polypeptides of the neck region to be projected in the same direction and toward the helical stalk (Fig. 2*A*). The neck domain also contains four experimentally confirmed N-linked glycans (54) attached to residue N149 on each protomer. Supporting cryo-EM densities of potential glycans were found in the vicinity of N149 in all four protomer neck structures (Fig. 2*A*). These glycans appear to shield the disulfide bridges between chains A–B and chains C–D. To characterize the potential functional role of these glycans for the stabilization of the asymmetric structure, we carried out molecular dynamics (MD) simulations of the fully glycosylated and deglycosylated head and neck H-protein. During the MD simulation of the fully glycosylated complex, the structure remained stable and glycans at N149 interacted extensively with the other protomers. When glycans were removed, the conformational space of the head and neck domains shifted away from that of the cryo-EM structure (*SI Appendix*, Fig. S5), indicating that glycosylation, in particular at N149, is important for stabilizing the asymmetric conformation observed in the cryo-EM structure. Finally, the neck of the CDV H-tetramer is bent by about 90°
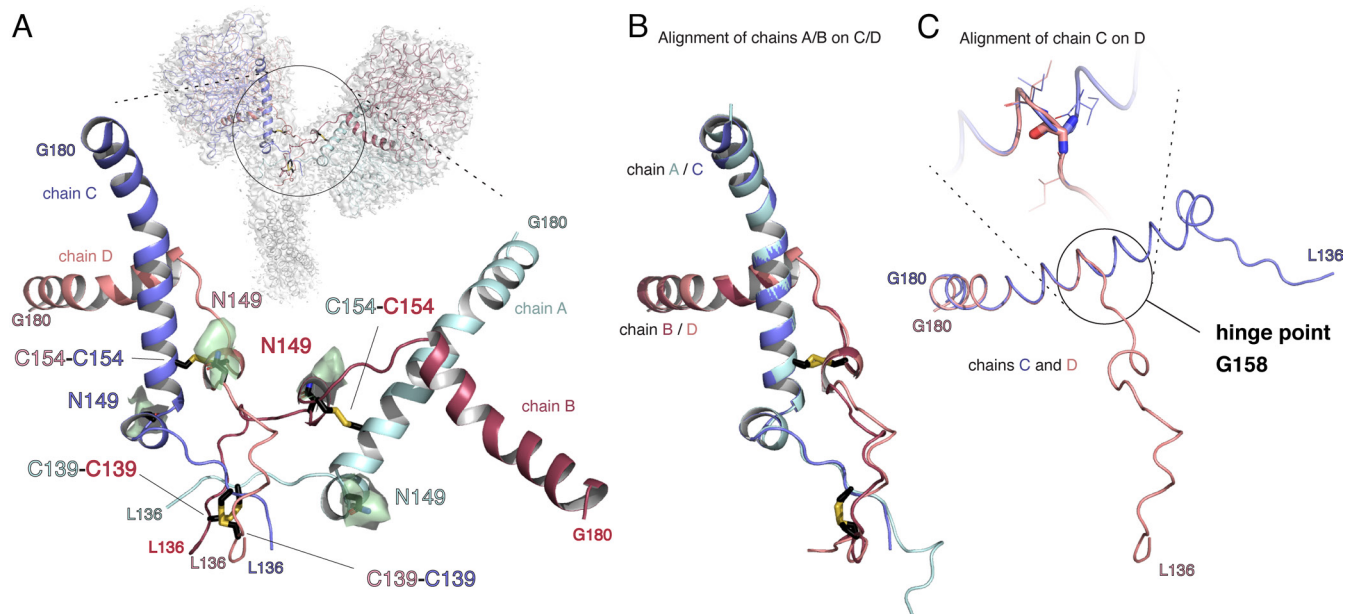
Fig. 2. Architecture of the CDV H-protein neck domain. (*A*) View into the neck region. To facilitate orientation within the neck, the whole tetrameric CDV attachment protein H-ectodomain structure and the last α-helix of the heads (the connector segment; *SI Appendix*, Fig. S2) are displayed. Structures are represented as cartoons and residues involved in disulfide bridge formation and N-glycosylation as sticks. Individual chains, disulfide bridges, and N-glycolsylation sites are labeled and color-coded as in Fig. 1. Cryo-EM density arising from N-glycosylations are shown in light green. The density is shown at a threshold level of 0.41 (3.00 σ). (*B*) Structural superposition of the neck/connector segments of chains A–D. Optimal alignment is found between chains A and C (mostly straight helix) and chains B and D (kinked loop). (*C*) Structural superposition of monomeric neck/connector segments of chains C and D. The hinge point at G158 in chain D is marked and viewed enlarged on top. In the cognate monomer C of the C/D dimer, no hinge point is observed. Hinge point glycine residues of chains C and D are shown as sticks and adjacent residues as lines and are color-coded as in Fig. 1.
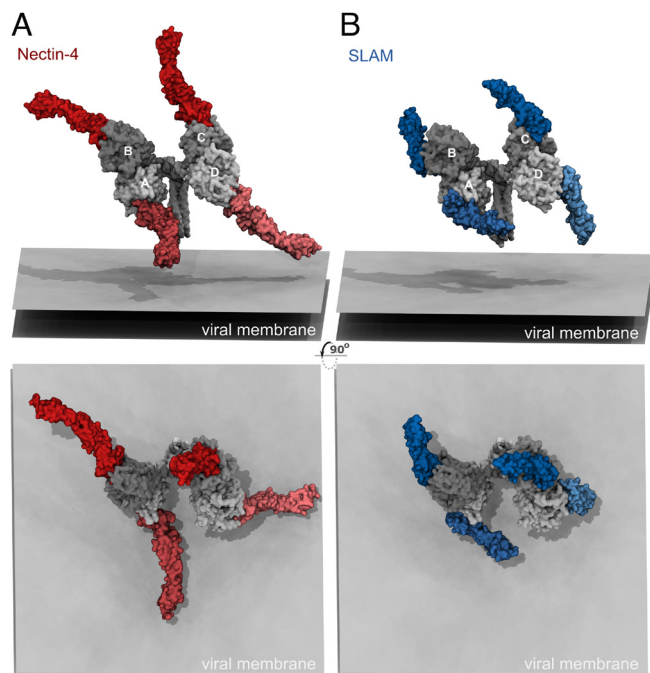
Fig. 3. Molecular docking of canine Nectin-4 (*A*) and SLAM (*B*) receptors to the tetrameric CDV H-protein ectodomain. CDV H-protein is displayed with shades of gray, and the viral membrane is represented by two gray planes intersecting the modeled transmembrane domain (not shown) at positions Y37 and V58. Nectin-4 (*A*) and SLAM (*B*) are shown in shades of red and blue, respectively. The color shade is scaled based on the distance from the viral membrane, i.e., lighter shades indicate closer proximity. The chains of the CDV H-protein protomers are marked in the images of the upper row. All proteins are displayed as space filling models.

with respect to the straight helical stalk, which results in both dimeric head units to be localized on one side of the CDV H-stalk (Fig. 1*B*). However, no interaction between the head and the stalk domains is visible.

Exposure of Receptor-Binding Sites on the Asymmetric CDV H-Tetramer. The cryo-EM structure of the CDV H-tetramer unveiled the specific spatial orientation of the two dimeric head domains that gives rise to the observed structural asymmetry. Molecular docking experiments were carried out in order to characterize how the asymmetric structure of the CDV H-tetramer would affect the binding of Nectin-4 and SLAM receptors (Fig. 3). In addition, docking allowed us to characterize and quantify the pairs of interacting residues between the H-protein and Nectin-4/SLAM protein (*SI Appendix*, Fig. S6). When the N-terminal region of the stalk points toward the viral membrane, only two of the four heads, i.e., chains B and C, point toward the extracellular solvent, allowing for an optimal engagement of the Nectin-4 and SLAM receptors. In contrast, the receptor bound to chain D is oriented directly toward the viral membrane, thus potentially hiding its accessibility and binding site. Finally, the receptor bound to chain A would be parallel to the viral membrane, which may impose structural constraints for optimal engagement of the receptor.

Discussion

Here, we report the structure and supramolecular organization of the entire apo tetrameric CDV H-ectodomain. One of the most unanticipated features of our apo CDV H-protein structure is the inherent asymmetric architecture. Such singular spatial organization originates from the neck domain, forming almost a 90° bent with respect to the straight helical stalk domain and thus

positioning the head domains to one side of the stalk. In addition, a hinge point at residue G158 in chains B and D of each H-dimer was identified and is necessary to direct both chains within a dimeric unit toward the compact four helical bundle stalk domain. When comparing the neck amino acid sequences of H-proteins from different morbilliviruses, it is evident that G158 and the immediate surrounding amino acids are unique to CDV (*SI Appendix*, Fig. S7). Glycine residues are known to play important roles providing structural flexibility at functionally important sites (56). Furthermore, we have previously shown that mutating G158 to alanine resulted in some defects in surface expression, suggesting suboptimal folding (57).

Reported biochemical and functional studies identified the stalk region of paramyxovirus receptor-binding proteins as the common domain that translates the signals received from head-mediated receptor engagement to F activation (24–29, 35, 36, 58–60). However, several variations of the mechanisms of F activation between different paramyxovirus members were suggested and supported by structural insights (20, 21). Head domains of the HN protein of parainfluenza virus type 5 (PIV5) (42) and Newcastle disease virus (NDV) (41), or the G protein of Nipah virus (NiV) (43), all cover a significant portion of their respective stalk domain (Fig. 4). In those three cases, it was proposed that head-mediated receptor engagement would expose previously hidden functional domains of the stalk to F interaction and activation (referred to as the "stalk-exposure" model) (58, 60, 61). Hence, productive NDV and PIV5 HN-stalk/F as well as NiV G-stalk/F interactions would occur after receptor binding, although an initial G-head/F binding mode was suggested for NiV prior to receptor engagement (59). For morbilliviruses, it was proposed that the F-protein already interacts with the H-stalk prior to receptor binding (29, 36, 39). Therefore, different from the stalk-exposure model, premature F activation would be prohibited by a specific pre-receptor-bound inhibitory conformation assumed by the H-protein (also referred to as the auto-repressed state) (29, 57). Receptor engagement would deactivate the auto-repressed state, thereby resulting in F activation at the right time and place (referred to as the "safety-catch" model) (29, 39, 57).

The asymmetric organization of the CDV H-tetrameric structure, where the dimeric head units are located on one side of the stalk, allows for a solvent-exposed interface of the stalk and thus provides the first structural insights supporting the safety-catch model. Prefusion F-trimers would be able to bind to the solvent-exposed side of the stalk without sterically clashing with the head domains even prior to contact with the receptor. Upon H-head receptor binding, deactivation of the auto-repressed state may involve structural rearrangements within the neck domain, which in turn, may unleash the inherent F activation function of the central portion of the stalk domain. Noteworthy, we recently demonstrated that substituting hydrophobic residues, i.e., isoleucine residues at positions 140 and 146 of the neck domain to polar or charged amino acids, led to non-functional tetrameric H-protein variants (57). The present structure reveals that residues 140 and 146 are part of the hydrophobic core of the neck domain (*SI Appendix*, Fig. S3). The introduction of polar or charged amino acids would thus have a disruptive effect that might either prevent H-folding into a productive pre-receptor-bound auto-repressed state and/or preclude conformational changes within the neck necessary to deactivate the H auto-repressed state.

Since the morbillivirus cell entry is assumed to be dynamic, it is plausible, from a mechanistic point of view, that alternative conformations of the H-protein might exist. However, we did not observe the presence of other conformations of H-protein in 3D classes. This would indicate that possible alternative conformations are energetically less stable than the one observed here or absent
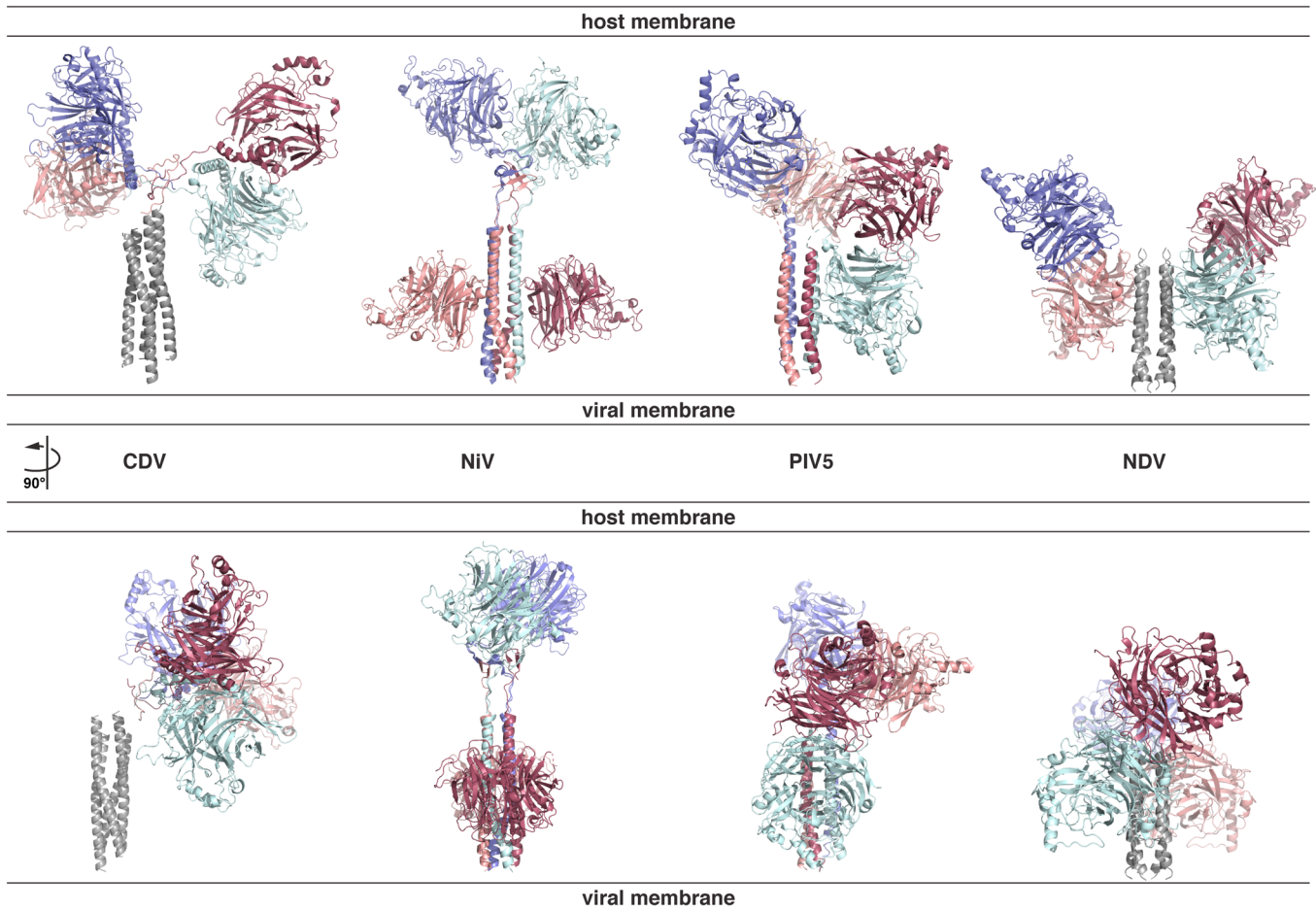
Fig. 4. Gallery of available paramyxovirus attachment protein structures. Structures are oriented such that the stalks are parallel to the viral membrane normal and viewed from two different sides. Note that only the here described CDV H-protein structure was captured in a conformation where the head dimers are positioned to one side of the stalk. Therefore, only opposing side of the stalk is exposed and could interact with fusion proteins. Structures are represented as cartoons and corresponding chains are colored according to Fig. 1. Unconnected stalk domains are colored in gray. Abbreviations: CDV (canine distemper virus), NiV (Nipah virus), PIV5 (parainfluenza virus 5), and NDV (Newcastle disease virus).

in our sample. Furthermore, the MD simulations, carried out under near physiological conditions, support that our CDV H-protein structure corresponds to a stable, low energy conformation (*SI Appendix*, Fig. S5). Since i) the H structure was determined in the absence of any bound ligands, ii) a large portion of the stalk domain would be accessible to F-protein interaction, and iii) the membrane-distal head domains expose their receptor-binding sites in a manner that may facilitate receptor-binding activity, we hypothesize that our cryo-EM CDV H-protein asymmetric structure may represent a biologically relevant conformation closely mimicking the auto-repressed state.

Collectively, in addition to contributing to refining our knowledge about the morbilliviral cell entry system, our CDV H-tetrameric structure represents a new blueprint for the structure-based design of next-generation antiviral drugs and vaccine candidates. In particular, structure-based protein engineering to further improve the overall stability of the H-tetramer, especially within the stalk and neck domains, may help pave the road to producing attractive immunogens necessary for antibody selection with broad-spectrum neutralizing activity or to generate new strategies to develop multivalent vaccines.

Methods

Expression and Purification of CDV H-Protein Ectodomain. In order to engineer the CDV H-protein ectodomain, we fused the following elements (N to C terminus): the mouse Ig Kappa signal peptide, a His/Twin-Strep-tag (62), a

tetrameric GCN4 motif (52), and the CDV H residues 60 to 607 (strain A75/17) (Fig. 1*D*). The CDV H-protein ectodomain construct was codon-optimized and protein produced at the protein-expression core facility of the École Polytechnique Fédérale de Lausanne (EPFL, Switzerland; Protein Production and Structure Core Facility). Briefly, ~2 × 10^9 expiCHO cells grown in suspension were transfected with 3 mg of expression plasmid. The supernatant (1 L) was harvested after 7 d of expression at 37 °C. Subsequently, the protein was purified from the supernatant using a 5 mL StrepTtrapXT column (Cytiva) and 100 mM Tris-HCl pH 8.0, 150 mM NaCl, and 1 mM ethylenediaminetetraacetic acid (EDTA) as buffer. Protein was eluted in the same buffer supplemented with 50 mM biotin (IBA-Lifesciences). The N-terminal His/Twin-Strep-tag was cleaved off using a two-molar excess of human rhinovirus 3C protease (BioVision) in the presence of 100 mM imidazole (4 h incubation at 4 °C). Cleaved CDV H-protein ectodomain was then concentrated using an Amicon Ultra (molecular weight cut-off 100 kDa) centrifugal filter (Millipore) and further purified by size-exclusion chromatography (SEC). Preparative SEC was performed at 8 °C on an Äkta Pure system (General Electric Healthcare) using a Superose 6 10/300 GL column (General Electric Healthcare) with TBS (Tris-buffered saline; 20 mM Tris-HCl pH 7.5, 100 mM NaCl) as running buffer. Peak fractions were pooled and concentrated to 1.5 mg/mL using an Amicon Ultra (molecular weight cut-off 100 kDa) centrifugal filter (Millipore) for cryo-EM grid preparation.

Cryo-EM Grid Preparation and Data Collection. Purified CDV H-protein ectodomain was diluted to 1.2 mg/mL in TBS containing 0.1% (w/v) β-D-octyl glucoside. Diluted protein sample was applied to Quantifoil R2/1 200 mesh copper holey-carbon grids that were glow discharged for 10 s at 10 mA and 0.25 mbar. Samples were blotted for 3.5 s and vitrified in liquid ethane using a Vitrobot Mark IV (Thermo Fisher) at 4 °C and 100% humidity. Data were acquired on a Titan Krios G3 (Thermo Fisher) operated at 300 kV and equipped with a Quantum-K3

direct electron detector (Gatan). Micrograph movies were recorded in counting mode at a magnification of 105,000× (corresponding to a calibrated pixel size of 0.822 Å) and a defocus range of −1.0 to −2.0 μm. A total of 26,339 movies from two different grids (two datasets) were collected. Movies were recorded for 1.5 s with a dose rate of 1.26 e⁻/Å²/frame, resulting in a total accumulated dose on the specimen level of approximately 50 e⁻/Å² per exposure.

Data Processing and Model Building. The single particle cryo-EM image processing workflow is summarized in *SI Appendix*, Fig. S8. Dose weighting and motion correction of dose-fractionated and gain-corrected movies were performed using MotionCor2 (version 1.4.0) (63). Contrast transfer function (CTF) parameters were estimated using CTFFIND4 (version 4.1.14) (64). Images displaying strong drift, astigmatism greater than 500 Å, and maximum CTF resolution worse than 6 Å were excluded from further processing (step 1 in *SI Appendix*, Fig. S8). A total of 6.47 million particles were picked using the Laplacian-of-Gaussian (LoG) filter in Relion (version 3.1.1) (65, 66) (step 2 in *SI Appendix*, Fig. S8). After three rounds of 2D classification and two rounds of 3D classification 1.14 million particles remained, which were subjected to Bayesian Polishing in Relion (version 3.1.1) (66) (steps 3 to 5 in *SI Appendix*, Fig. S8). The two datasets were processed independently up to this point (Grid1 and Grid2, and step "particles pooled" in *SI Appendix*, Fig. S8). The polished particles were imported in cryoSPARC (cryo-EM Single Particle Ab-initio Reconstruction and Classification; version 3.2) (67) and pooled for the following processing steps: A final 2D classification run was performed with these pooled particle sets resulting in 882,527 particle picks (step 6 in *SI Appendix*, Fig. S8). Ab initio reconstruction in cryoSPARC (version 3.2) (67) (step 7 in *SI Appendix*, Fig. S8) always yielded three different types of volumes regardless of the number of classes used as input: a volume with the heads only, one with the heads and the neck, and another one with all three parts, i.e., heads, neck, and stalk. All three types of H-tetrameric volumes indicated similar arrangement of the heads, i.e., only one conformation. Heterogeneous refinement in cryoSPARC (version 3.2) (67) was performed with these three types of volumes (marked by asterisks in step 7 of *SI Appendix*, Fig. S8) and all 882,526 particles (boxed volumes in step 7 of *SI Appendix*, Fig. S8). The particles that only contained information about the head domains resulted in the volume with the lowest resolution and were excluded in subsequent processing steps. The resulting 663,258 particles (boxed volumes in step 8 of *SI Appendix*, Fig. S8) and the 3D map showing the heads, neck, and the stalk (marked by an asterisks in step 8 of *SI Appendix*, Fig. S8) were further refined by non-uniform refinement, a global and local CTF refinement, another non-uniform refinement, and a final local refinement in cryoSPARC (version 3.2) (67) (steps 9 to 12 in *SI Appendix*, Fig. S8). Homology model of CDV H-protein ectodomain was generated by SWISS-MODEL (68) based on the biological assembly of the MeV hemagglutinin X-ray structure (PDB-ID: 2ZB6), which is a dimer. Two homology model dimers were manually placed and fitted into the volume representing the heads of the final sharpened map using UCSF Chimera v1.12 (University of California, San Francisco Chimera) (69). The neck was completely built de novo in Coot (70). The local resolution in the C-terminal region of the stalk domain and the N-terminal region of the neck domain was not sufficient to trace the protein main chain with confidence. Thus, for the stalk domain, four poly-alanine α-helices were placed into the stalk volume of the unsharpened map and real space refined with the sharpened map (*SI Appendix*, Fig. S9) in Coot (70). The final protein model (residues 130 (chain A)/134 (chain B)/136 (chain C)/133 (chain D) to 602 (chains A–D) was obtained by several iterations of manual model building in Coot (70), real-space refinement in Phenix (version 1.19) (71), and structure validation using MolProbity (72). Data collection, refinement, and validation statistics are summarized in *SI Appendix*, Table S1, and analysis of the final cryo-EM density map is shown in *SI Appendix*, Fig. S10. The cryo-EM map and the protein coordinates were deposited in the Electron Microscopy Data Bank (EMD-14842) and Protein Data Bank (PDB-ID: 7ZNY), respectively. All volume and structural representations were prepared using UCSF ChimeraX v1.3 (73) or PyMol v2.5.2 (The PyMol Molecular Graphics System, Schrödinger).

Molecular Dynamics (MD) Simulations. MD simulations were conducted to characterize the stability of the asymmetric H-protein tetramer structure. Two systems were investigated: the fully glycosylated and deglycosylated structure of the H-protein. For the fully glycosylated structure, N-linked mannose-5 glycans (Man5) were modeled onto sequons N149, N391, N422, N456, and N587 using the Python package Glycosylator (74). Both structures were then solvated in a 20 Å padding water box and neutralized with 150 mM NaCl. The simulations were performed with the CHARMM36 (Chemistry at HARvard Macromolecular Mechanics 36) force field (75), including CMAP corrections for the protein. The water molecules were described with the TIP3P (transferable intermolecular potential with 3 points) water (76) parameterization. The simulations were carried out with OPENMM molecular engine (77). The systems were first minimized for 5,000 steps followed by an equilibration (1.75 ns), progressively releasing positional restraints on the backbone atoms. The cutoff for non-bonded interactions was set to 12 Å with a switching distance at 10 Å. The periodic electrostatic interactions were computed using Particle-Mesh Ewald summation with a grid spacing smaller than 1 Å. Constant temperature of 300 K was imposed by Langevin dynamics with a damping coefficient of 1.0 ps. Constant pressure of 1 atm was maintained with Monte Carlo barostat (78). The hydrogen mass repartitioning scheme was used to achieve a 4 fs time-step (79). Snapshots from each simulation were extracted at 1 ns time intervals for structural analysis. The principal component analysis was carried out using ProDy (80).

Molecular Docking. Protein–protein docking was used to investigate the binding between CDV H-protein and the canine receptors Nectin-4 and SLAM. The Alphafold 2.0 structural models of Nectin-4 and SLAM were downloaded from Uniprot (AF-K4Q246-F1 and AF-Q95MM9-F1, respectively). Residues 31 to 145 were then isolated for Nectin-4 and residues 31 to 140 for SLAM. The RosettaDock (2020.08.6114) procedure was used for the protein–protein docking (81). The docking experiments were seeded based on the experimental structures of Nectin-4 [PDB-ID: 4GJT (34)] and SLAM [PDB-ID: 3ALZ (33)] bound to the homologous MeV H-protein. Both receptors were docked separately onto each protomer of the CDV H-protein. For each protomer, 500 poses were generated. The poses with the lowest energy and the smallest RMSD to the related MeV experimental structure were considered as a successful docked complex. The chosen complexes were then minimized with the fast relax procedure of Rosetta. The interface energies were computed with the "interface_energy" function of Rosetta. The transmembrane and stalk were modeled with Alphafold colab (82). Images were rendered with VMD (visual molecular dynamics) (83).

Data, Materials, and Software Availability. The atomic coordinates of the CDV H-protein ectodomain structure have been deposited in the Protein Data Bank (PDB; https://www.rcsb.org) under PDB-ID: 7ZNY.

Author affiliations: ᵃInstitute of Biochemistry and Molecular Medicine, Medical Faculty, University of Bern, CH-3012 Bern, Switzerland; ᵇDivision of Neurological Sciences, Vetsuisse Faculty, University of Bern, CH-3001 Bern, Switzerland; and ᶜInstitute of Chemistry and Biotechnology, Competence Center for Drug Discovery, Zurich University of Applied Sciences, CH-8820 Wädenswil, Switzerland

Author contributions: D.K., J.-M.J., T.L., P.P., and D.F. designed research; D.K., J.-M.J., M.W., and T.L. performed research; N.S., D.P., R.R., T.L., P.P., and D.F. contributed new reagents/analytic tools; D.K., J.-M.J., N.S., D.P., R.R., T.L., P.P., and D.F. analyzed data; and D.K., J.-M.J., N.S., D.P., R.R., T.L., P.P., and D.F. wrote the paper.

1. M. K. Patel *et al.*, Progress toward regional measles elimination - worldwide, 2000–2019. *MMWR Morb. Mortal Wkly Rep.* **69**, 1700–1705 (2020).
2. T. E. Amundson, T. M. Yuill, Prevalence of selected pathogenic microbial agents in the red fox (*Vulpes fulva*) and gray fox (*Urocyon cinereoargenteus*) of southwestern Wisconsin. *J. Wildl. Dis.* **17**, 17–22 (1981).
3. A. D. Osterhaus *et al.*, Canine distemper virus in seals. *Nature* **335**, 403–404 (1988).
4. M. E. Roelke-Parker *et al.*, A canine distemper virus epidemic in Serengeti lions (*Panthera leo*). *Nature* **379**, 441–445 (1996).
5. L. Haas *et al.*, Canine distemper virus infection in Serengeti spotted hyenas. *Vet. Microbiol.* **49**, 147–152 (1996).
6. E. W. Uhl *et al.*, New world origin of canine distemper: Interdisciplinary insights. *Int. J. Paleopathol.* **24**, 266–278 (2019).

7. A. Beineke, S. Markus, J. Borlak, T. Thum, W. Baumgartner, Increase of pro-inflammatory cytokine expression in non-demyelinating early cerebral lesions in nervous canine distemper. *Viral. Immunol.* **21**, 401–410 (2008).

8. A. Beineke, C. Puff, F. Seehusen, W. Baumgartner, Pathogenesis and immunopathology of systemic and nervous canine distemper. *Vet. Immunol. Immunopathol.* **127**, 1–18 (2009).

9. C. Lempp et al., New aspects of the pathogenesis of canine distemper leukoencephalitis. *Viruses* **6**, 2571–2601 (2014).

10. L. Roberts, Pandemic brings mass vaccinations to a halt. *Science* **368**, 116–117 (2020).

11. K. Sakai et al., Lethal canine distemper virus outbreak in cynomolgus monkeys in Japan in 2008. *J. Virol.* **87**, 1105–1114 (2013).

12. N. Feng et al., Fatal canine distemper virus infection of giant pandas in China. *Sci. Rep.* **6**, 27518 (2016).

13. Y. Jin et al., Canine distemper viral infection threatens the giant panda population in China. *Oncotarget* **8**, 113910–113919 (2017).

14. S. Liu et al., Mortality analysis of captive red panda cubs within Chengdu, China. *BMC Vet. Res.* **18**, 68 (2022).

15. H. Tatsuo, N. Ono, K. Tanaka, Y. Yanagi, SLAM (CDw150) is a cellular receptor for measles virus. *Nature* **406**, 893–897 (2000).

16. H. Tatsuo, N. Ono, Y. Yanagi, Morbilliviruses use signaling lymphocyte activation molecules (CD150) as cellular receptors. *J. Virol.* **75**, 5842–5850 (2001).

17. C. Erlenhoefer et al., CD150 (SLAM) is a receptor for measles virus but is not involved in viral contact-mediated proliferation inhibition. *J. Virol.* **75**, 4499–4505 (2001).

18. R. S. Noyce et al., Tumor cell marker PVRL4 (nectin 4) is an epithelial cell receptor for measles virus. *PLoS Pathog.* **7**, e1002240 (2011).

19. M. D. Mühlebach et al., Adherens junction protein nectin-4 is the epithelial receptor for measles virus. *Nature* **480**, 530–533 (2011).

20. P. Plattet, L. Alves, M. Herren, H. C. Aguilar, Measles virus fusion protein: Structure, function and inhibition. *Viruses* **8**, 112 (2016).

21. C. K. Navaratnarajah, A. R. Generous, I. Yousaf, R. Cattaneo, Receptor-mediated cell entry of paramyxoviruses: Mechanisms, and consequences for tropism and pathogenesis. *J. Biol. Chem.* **295**, 2771–2786 (2020).

22. T. Hashiguchi et al., Structures of the prefusion form of measles virus fusion protein in complex with inhibitors. *Proc. Natl. Acad. Sci. U.S.A.* **115**, 2496–2501 (2018).

23. D. Kalbermatter et al., Cryo-EM structure of the prefusion state of canine distemper virus fusion protein ectodomain. *J. Struct. Biol. X* **4**, 100021 (2020).

24. N. Ader et al., Structural rearrangements of the central region of the Morbillivirus attachment protein stalk domain trigger F protein refolding for membrane fusion. *J. Biol. Chem.* **287**, 16324–16334 (2012).

25. M. A. Brindley, M. Takeda, P. Plattet, R. K. Plemper, Triggering the measles virus membrane fusion machinery. *Proc. Natl. Acad. Sci. U.S.A.* **109**, E3018–E3027 (2012).

26. C. K. Navaratnarajah, S. Negi, W. Braun, R. Cattaneo, Membrane fusion triggering: Three modules with different structure and function in the upper half of the measles virus attachment protein stalk. *J. Biol. Chem.* **287**, 38543–38551 (2012).

27. S. Apte-Sengupta, C. K. Navaratnarajah, R. Cattaneo, Hydrophobic and charged residues in the central segment of the measles virus hemagglutinin stalk mediate transmission of the fusion-triggering signal. *J. Virol.* **87**, 10401–10404 (2013).

28. C. K. Navaratnarajah et al., The measles virus hemagglutinin stalk: Structures and functions of the central fusion activation and membrane-proximal segments. *J. Virol.* **88**, 6158–6167 (2014).

29. N. Ader-Ebert et al., Sequential conformational changes in the Morbillivirus attachment protein initiate the membrane fusion process. *PLoS Pathog* **11**, e1004880 (2015).

30. L. A. Colf, Z. S. Juo, K. C. Garcia, Structure of the measles virus hemagglutinin. *Nat. Struct. Mol. Biol.* **14**, 1227–1228 (2007).

31. T. Hashiguchi et al., Crystal structure of measles virus hemagglutinin provides insight into effective vaccines. *Proc. Natl. Acad. Sci. U.S.A.* **104**, 19535–19540 (2007).

32. C. Santiago, M. L. Celma, T. Stehle, J. M. Casasnovas, Structure of the measles virus hemagglutinin bound to the CD46 receptor. *Nat. Struct. Mol. Biol.* **17**, 124–129 (2009).

33. T. Hashiguchi et al., Structure of the measles virus hemagglutinin bound to its cellular receptor SLAM. *Nat. Struct. Mol. Biol.* **18**, 135–141 (2011).

34. X. Zhang et al., Structure of measles virus hemagglutinin bound to its epithelial receptor nectin-4. *Nat. Struct. Mol. Biol.* **20**, 67–72 (2013).

35. J. K. Lee et al., Functional interaction between paramyxovirus fusion and attachment proteins. *J. Biol. Chem.* **283**, 16561–16572 (2008).

36. M. A. Brindley et al., A stabilized headless measles virus attachment protein stalk efficiently triggers membrane fusion. *J. Virol.* **87**, 11693–11703 (2013).

37. R. K. Plemper, A. L. Hammond, R. Cattaneo, Measles virus envelope glycoproteins hetero-oligomerize in the endoplasmic reticulum. *J. Biol. Chem.* **276**, 44239–44246 (2001).

38. T. Paal et al., Probing the spatial organization of measles virus fusion complexes. *J. Virol.* **83**, 10480–10493 (2009).

39. M. A. Brindley, S. Chaudhury, R. K. Plemper, Measles virus glycoprotein complexes preassemble intracellularly and relax during transport to the cell surface in preparation for fusion. *J. Virol.* **89**, 1230–1241 (2015).

40. M. Aggarwal, R. K. Plemper, Structural insight into paramyxovirus and pneumovirus entry inhibition. *Viruses* **12**, 342 (2020).

41. P. Yuan et al., Structure of the Newcastle disease virus hemagglutinin-neuraminidase (HN) ectodomain reveals a four-helix bundle stalk. *Proc. Natl. Acad. Sci. U.S.A.* **108**, 14920–14925 (2011).

42. B. D. Welch et al., Structure of the parainfluenza virus 5 (PIV5) hemagglutinin-neuraminidase (HN) ectodomain. *PLoS Pathog* **9**, e1003534 (2013).

43. Z. Wang et al., Architecture and antigenicity of the Nipah virus attachment glycoprotein. *Science* **375**, 1373–1378 (2022).

44. V. von Messling, C. Springfeld, P. Devaux, R. Cattaneo, A ferret model of canine distemper virus virulence and immunosuppression. *J. Virol.* **77**, 12579–12591 (2003).

45. F. Bonami, P. A. Rudd, V. von Messling, Disease duration determines canine distemper virus neurovirulence. *J. Virol.* **81**, 12066–12070 (2007).

46. S. Pillet, N. Svitek, V. von Messling, Ferrets as a model for morbillivirus pathogenesis, complications, and vaccines. *Curr. Top Microbiol. Immunol.* **330**, 73–87 (2009).

47. R. N. Rouxel, N. Svitek, V. von Messling, A chimeric measles virus with canine distemper envelope protects ferrets from lethal distemper challenge. *Vaccine* **27**, 4961–4966 (2009).

48. W. Li et al., Genetic characterization of an isolate of canine distemper virus from a Tibetan Mastiff in China. *Virus Genes* **49**, 45–57 (2014).

49. T. Enkirch, V. von Messling, Ferret models of viral pathogenesis. *Virology* **479–480**, 259–270 (2015).

50. R. da Fontoura Budaszewski, V. von Messling, Morbillivirus experimental animal models: Measles virus pathogenesis insights from canine distemper virus. *Viruses* **8**, 274 (2016).

51. B. Sawatsky, R. Cattaneo, V. von Messling, Canine distemper virus spread and transmission to naive ferrets: Selective pressure on signaling lymphocyte activation molecule-dependent entry. *J. Virol.* **92**, e00669–18 (2018).

52. P. B. Harbury, T. Zhang, P. S. Kim, T. Alber, A switch between two-, three-, and four-stranded coiled coils in GCN4 leucine zipper mutants. *Science* **262**, 1401–1407 (1993).

53. P. R. Mittl et al., The retro-GCN4 leucine zipper sequence forms a stable three-dimensional structure. *Proc. Natl. Acad. Sci. U.S.A.* **97**, 2562–2566 (2000).

54. B. Sawatsky, V. von Messling, Canine distemper viruses expressing a hemagglutinin without N-glycans lose virulence but retain immunosuppression. *J. Virol.* **84**, 2753–2761 (2010).

55. E. Krissinel, K. Henrick, Inference of macromolecular assemblies from crystalline state. *J. Mol. Biol.* **372**, 774–797 (2007).

56. B. X. Yan, Y. Q. Sun, Glycine residues provide flexibility for enzyme active sites. *J. Biol. Chem.* **272**, 3190–3194 (1997).

57. M. Herren, N. Shrestha, M. Wyss, A. Zurbriggen, P. Plattet, Regulatory role of the morbillivirus attachment protein head-to-stalk linker module in membrane fusion triggering. *J. Virol.* **92**, e00679–18 (2018).

58. S. Bose et al., Fusion activation by a headless parainfluenza virus 5 hemagglutinin-neuraminidase stalk suggests a modular mechanism for triggering. *Proc. Natl. Acad. Sci. U.S.A.* **109**, E2625–E2634 (2012).

59. Q. Liu et al., Unraveling a three-step spatiotemporal mechanism of triggering of receptor-induced Nipah virus fusion and cell entry. *PLoS Pathog.* **9**, e1003770 (2013).

60. S. Bose, A. S. Song, T. S. Jardetzky, R. A. Lamb, Fusion activation through attachment protein stalk domains indicates a conserved core mechanism of paramyxovirus entry into cells. *J. Virol.* **88**, 3925–3941 (2014).

61. S. Bose, T. S. Jardetzky, R. A. Lamb, Timing is everything: Fine-tuned molecular machines orchestrate paramyxovirus entry. *Virology* **479–480**, 518–531 (2015).

62. D. Wrapp et al., Cryo-EM structure of the 2019-nCoV spike in the prefusion conformation. *Science* **367**, 1260–1263 (2020).

63. S. Q. Zheng et al., MotionCor2: Anisotropic correction of beam-induced motion for improved cryo-electron microscopy. *Nat. Methods* **14**, 331–332 (2017).

64. A. Rohou, N. Grigorieff, CTFFIND4: Fast and accurate defocus estimation from electron micrographs. *J. Struct. Biol.* **192**, 216–221 (2015).

65. S. H. Scheres, RELION: Implementation of a Bayesian approach to cryo-EM structure determination. *J. Struct. Biol.* **180**, 519–530 (2012).

66. J. Zivanov et al., New tools for automated high-resolution cryo-EM structure determination in RELION-3. *Elife* **7**, e42166 (2018).

67. A. Punjani, J. L. Rubinstein, D. J. Fleet, M. A. Brubaker, cryoSPARC: Algorithms for rapid unsupervised cryo-EM structure determination. *Nat. Methods* **14**, 290–296 (2017).

68. A. Waterhouse et al., SWISS-MODEL: Homology modelling of protein structures and complexes. *Nucleic Acids Res.* **46**, W296–W303 (2018).

69. E. F. Pettersen et al., UCSF Chimera–a visualization system for exploratory research and analysis. *J. Comput. Chem.* **25**, 1605–1612 (2004).

70. P. Emsley, B. Lohkamp, W. G. Scott, K. Cowtan, Features and development of Coot. *Acta Crystallogr. D Biol. Crystallogr.* **66**, 486–501 (2010).

71. P. V. Afonine et al., Real-space refinement in PHENIX for cryo-EM and crystallography. *Acta Crystallogr. D Struct. Biol.* **74**, 531–544 (2018).

72. C. J. Williams et al., MolProbity: More and better reference data for improved all-atom structure validation. *Protein Sci.* **27**, 293–315 (2018).

73. E. F. Pettersen et al., UCSF ChimeraX: Structure visualization for researchers, educators, and developers. *Protein Sci.* **30**, 70–82 (2021).

74. T. Lemmin, C. Soto, Glycosylator: A Python framework for the rapid modeling of glycans. *BMC Bioinf.* **20**, 513 (2019).

75. R. B. Best et al., Optimization of the additive CHARMM all-atom protein force field targeting improved sampling of the backbone phi, psi and side-chain chi(1) and chi(2) dihedral angles. *J. Chem. Theory Comput.* **8**, 3257–3273 (2012).

76. W. L. Jorgensen, J. Chandrasekhar, J. D. Madura, R. W. Impey, M. L. Klein, Comparison of simple potential functions for simulating liquid water. *J. Chem. Phys.* **79**, 926 (1983).

77. P. Eastman et al., OpenMM 7: Rapid development of high performance algorithms for molecular dynamics. *PLoS Comput. Biol.* **13**, e1005659 (2017).

78. K.-H. Chow, D. M. Ferguson, Isothermal-isobaric molecular dynamics simulations with Monte Carlo volume sampling. *Comput. Phys. Commun.* **91**, 283–280 (1995).

79. C. Balusek et al., Accelerating membrane simulations with hydrogen mass repartitioning. *J. Chem. Theory Comput.* **15**, 4673–4686 (2019).

80. A. Bakan, L. M. Meireles, I. Bahar, ProDy: Protein dynamics inferred from theory and experiments. *Bioinformatics* **27**, 1575–1577 (2011).

81. S. Chaudhury et al., Benchmarking and analysis of protein docking performance in Rosetta v3.2. *PLoS One* **6**, e22477 (2011).

82. M. Mirdita et al., ColabFold: Making protein folding accessible to all. *Nat. Methods* **19**, 679–682 (2022).

83. W. Humphrey, A. Dalke, K. Schulten, VMD: Visual molecular dynamics. *J. Mol. Graph* **14**, 27–28 (1996).